

The transmission spectrum of WASP-17 b from the optical to the near-infrared wavelengths: combining STIS, WFC3 and IRAC datasets

ARIANNA SABA,¹ ANGELOS TSIARAS,¹ MARIO MORVAN,¹ ALEXANDRA THOMPSON,¹ QUENTIN CHANGEAT,¹ BILLY EDWARDS,¹
ANDREW JOLLY,^{1,2} INGO WALDMANN,¹ AND GIOVANNA TINETTI¹

¹*Department of Physics and Astronomy, University College London, Gower Street, WC1E 6BT London, United Kingdom*

²*School of Physics, University of New South Wales, Sydney, NSW 2052, Australia*

ABSTRACT

We present the transmission spectrum of the inflated hot-Jupiter WASP-17 b, observed with the STIS (grisms G430L, G750L) and WFC3 (grisms G102, G141) instruments aboard the Hubble Space Telescope, allowing for a continuous wavelength coverage from ~ 0.4 to ~ 1.7 μm . Available observations taken with IRAC channel 1 and 2 on the Spitzer Space Telescope are also included, adding photometric measurements at 3.6 and 4.5 μm . HST spectral data was analysed with the open-source pipeline Iraclis, which is specialised on the reduction of STIS and WFC3 transit and eclipse observations. Spitzer photometric observations were reduced with the TLCD-LSTM (Transit Light Curve Detrending LSTM) method, which employs recurrent neural networks to predict the correlated noise and detrend Spitzer transit lightcurves. The outcome of our reduction produces incompatible results between STIS visit 1 and visit 2, which leads us to consider two scenarios for G430L. Additionally, by modelling the WFC3 data alone, we can extract atmospheric information without having to deal with the contrasting STIS datasets. We run separate retrievals on the three spectral scenarios with the aid of TauREx3, a fully Bayesian retrieval framework. We find that, independently of the data considered, the exoplanet atmosphere displays strong water signatures, aluminium oxide (AlO) and titanium hydride (TiH). A retrieval that includes an extreme photospheric activity of the host star is the preferred model, but we recognise that such scenario is unlikely for an F6-type star. Due to the incompleteness of all STIS spectral lightcurves, only further observations with this instrument would allow us to properly constrain the atmospheric limb of WASP-17 b, before JWST or Ariel will come online.

1. INTRODUCTION

In recent years, the *Hubble Space Telescope* has been at the forefront of exoplanet atmospheric characterisation. Thanks to its Wide Field Camera 3 (WFC3) and its Space Telescope Imaging Spectrograph (STIS), often combined with the InfraRed Array Camera (IRAC) aboard the *Spitzer Space Telescope*, the atmosphere of hot-Jupiters (Skaf et al. 2020; Pluriel et al. 2020b; Sing et al. 2016; Tsiaras et al. 2018; Pinhas et al. 2018), ultra-hot-Jupiters (Edwards et al. 2020a; Kreidberg et al. 2018; Changeat et al. 2020; Mikal-Evans et al. 2019), super-Earths (Edwards et al. 2020b; Tsiaras et al. 2016b, 2019; Mugnai et al. 2021), sub-Neptunes (Guo et al. 2020; Guilluy et al. 2020) and hot-Saturns (Carone et al. 2021; Anisman et al. 2020) have been studied in transmission, emission and across their phase-curves (Stevenson et al. 2017; Changeat et al. 2021; Kreidberg et al. 2018; Irwin et al. 2020; Feng et al. 2020; Arcangeli et al. 2019). Although small rocky planets are difficult to probe with current spectrographs due to the limited

signal to noise ratio of their gaseous envelope, atmospheric studies conducted on extrasolar gas giants reported the detection of various molecules, in particular water vapour.

Among the exoplanet population of inflated hot-Jupiters, WASP-17 b (Anderson et al. 2010) is one of the least dense planets discovered so far, with a radius equal to $1.87 \pm 0.24 R_J$ (Southworth et al. 2012) and a mass 0.78 times that of Jupiter (Stassun et al. 2017). The transiting planet, confirmed to possess a retrograde orbit (Bayliss et al. 2010; Hébrard et al. 2011; Simpson et al. 2011), forms an angle of $148.5^\circ \pm_{4.2}^{5.1}$ with respect to the rotation axis of its parent star (Triaud et al. 2010). The considerable orbital obliquity of WASP-17 b cannot be explained by inward migration (Lin et al. 1996; Ida & Lin 2004) but could be rather due to an initial misalignment between the star and the protoplanetary disk (Bate et al. 2010), planet-planet scattering or the Kozai mechanism (Nagasawa et al. 2008). These processes also induce the very small eccentricities reported in orbitally

misaligned planets (Bourrier et al. 2018; Johnson et al. 2009; Winn et al. 2009): in fact, Southworth et al. (2012) were not able to find any evidence of the orbital eccentricity of WASP-17 b. The exoplanet takes 3.7 days to orbit its host star (Southworth et al. 2012), a F6-type star with $V_{mag}=11.6$ (Anderson et al. 2010).

Given the planet’s very large atmospheric scale height (Anderson et al. 2010), transmission spectroscopy studies have been extremely successful. From the ground, sodium was detected at optical wavelengths by Wood et al. (2011) and Zhou & Bayliss (2012) using the VLT, and with the Magellan Telescope by Khalafinejad et al. (2018). At low-resolution, the spectrograph FORS2 mounted on the VLT detected potassium in the atmosphere of WASP-17b with a 3σ significance and water absorption (Sedaghati et al. 2016a). From space, data taken with HST in the optical and near-infrared and with Spitzer at 3.6 μm and 4.5 μm , report water absorption and alkali features, with little to no clouds/hazes (Sing et al. 2016). A similar study conducted by Barstow et al. (2016) also reports the presence of water at solar abundances in the limb of WASP-17b, possibly accompanied by CO signatures. However, contrary to the results by Sing et al. (2016), their best atmospheric model includes scattering aerosols at relatively high altitudes, up to 1 mbar.

Here we present the spectroscopic analysis performed on transit observations taken with STIS (grisms G430L and G750L) and WFC3 (grisms G102 and G141) onboard the *Hubble Space Telescope* and with IRAC channel 1 and 2 of the *Spitzer Space Telescope*. The combination of the aforementioned instruments allows us to investigate the spectrum of WASP-17 b from the optical to the near infrared wavelengths (0.4 - 5 μm).

2. METHODOLOGY

2.1. HST data processing

2.1.1. WFC3

We downloaded the HST/WFC3 raw spectroscopic and spatially scanned observations of WASP-17 b from the Mikulski Archive for Space Telescopes (MAST), as part of the HST Proposal 14918 (P.I. Hannah Wakeford).

Two transits of the exoplanet were observed with the grisms G102 and G141, which cover the wavelengths between 0.8 - 1.1 μm and 1.1 - 1.7 μm respectively. We employed Iraclis (Tsiaras et al. 2016a), an open-source reduction pipeline for WFC3¹, to reduce the data and extract the lightcurves by performing the following steps:

¹ <https://github.com/ucl-exoplanets/Iraclis>

Table 1. Stellar and planetary parameters for WASP-17 b used for the data reduction with Iraclis and TLCD-LSTM, and the atmospheric modelling with TauREx3.

Stellar & Planetary Parameters	
T_* [K]	6550 ± 100 *
R_* [R_\odot]	$1.573^{+0.084}_{-0.092}$ †
M_* [M_\odot]	$1.35^{+0.27}_{-0.16}$ †
$\log_{10}(g)$ [cm/s^2]	4.24 ± 0.13 *
[Fe/H]	-0.25 ± 0.09 *
a/R_*	$7.27^{+0.21}_{-0.44}$
e	0 (fixed)
i [$^\circ$]	$87.96^{+1.34}_{-1.56}$
ω	0 (fixed)
P [days]	$3.7354845 \pm 1.9 \times 10^{-6}$ †
T_0 [BJD_{TDB}]	2454592.8015 ± 0.0005 †
R_p/R_*	0.1235 ± 0.0011 ‡
M_p [M_J]	0.780 ± 0.230 †
R_p [R_J]	1.87 ± 0.24 †

* Anderson et al. (2010)
† Southworth et al. (2012)
‡ Sedaghati et al. (2016b)
† Stassun et al. (2017)
† Stassun et al. (2019)

zero-read subtraction, reference pixels correction, non-linearity correction, dark current subtraction, gain conversion, sky background subtraction, calibration, flat-field correction, bad pixels and cosmic rays correction, and lightcurve extraction. Further information on Iraclis can be found in Tsiaras et al. (2016a,b, 2018).

2.1.2. STIS

We downloaded the HST/STIS raw spectroscopic observations of WASP-17 b from the Mikulski Archive for Space Telescopes (MAST), as part of the HST Proposal 12473 (P.I. David Sing).

Three transits of the exoplanet were observed with the grisms G430L (two transits) and G750L (one transit), which cover the wavelengths between 0.3 - 0.57 μm and 0.5 - 0.94 μm respectively. For the analysis of these data sets we used again Iraclis but adapted most of the reduction steps to STIS. These steps are: bias level subtraction, bias correction image subtraction, dark image subtraction, flat field correction, calibration, background subtraction, bad pixels and cosmic rays correction, and lightcurve extraction. The first five steps were performed following the recipes described in the STIS Handbook (Bostroem & Proffitt 2011), while the rest were implemented in the same way as for the WFC3 staring-mode observations. For the extraction we used 6-pixel-wide apertures along the cross-dispersion direc-

tion and smoothed aperture edges along the dispersion direction (the smoothing factors were 5 Å for the G430L grism and 10 Å for the G750L grism, corresponding to approximately two pixels in each case).

2.2. HST lightcurve modelling

Table 1 summarises the parameters used for the lightcurve modelling. For these parameters we consulted the Exoplanet Characterisation Catalogue developed as part of the ExoClock project (Kokori et al. 2021). In all the lightcurve modelling steps we assumed a circular orbit and a fixed period for the planet, while the limb-darkening effect was modelled using the Claret 4-coefficient law (Claret 2000) and the ExoTETHyS (Morello et al. 2020) package which takes into account the stellar parameters (Table 1) and the response curve of the instrument.

At a first stage, the initial orbit of each HST visit was discarded since it presents more significant wavelength-dependent systematics compared to the subsequent orbits. We then analysed only the white lightcurves (broad-band) and let the semi-major axis, the inclination, the mid-transit time and the R_p/R_* as free parameters, together with a number of parameters for the systematics implemented in Iraclis.

To ensure consistency between the analysis of the different data sets, we estimated again the inclination and the semi-major axis of the planet using all the available data. We combined the lightcurves extracted from the five HST observations, together with five TESS (Ricker et al. 2014) observations. The updated parameters are reported in Table 1.

Finally, we analysed all the white and spectral HST lightcurves fixing the values for the semi-major axis and the inclination. Figures 1, 2, 3, 4 and 5 show the fitted white and spectral lightcurves for all the HST observations.

2.3. Spitzer data analysis

Spitzer data is available on the IRSA online archive. We downloaded the WASP-17b transit observations taken with IRAC channel 1 and 2 in 2013 (P.I. Jean-Michel Desert, programme 90092). The two observations were analysed separately by employing the lightcurve detrending method named TLCD-LSTM² developed by Morvan et al. (2020). This approach uses a Long Short-Term Memory network (Hochreiter & Schmidhuber 1997) to predict the transit lightcurve without the need for any prior assumptions on the noise or transit shape. The only assumption regarding the

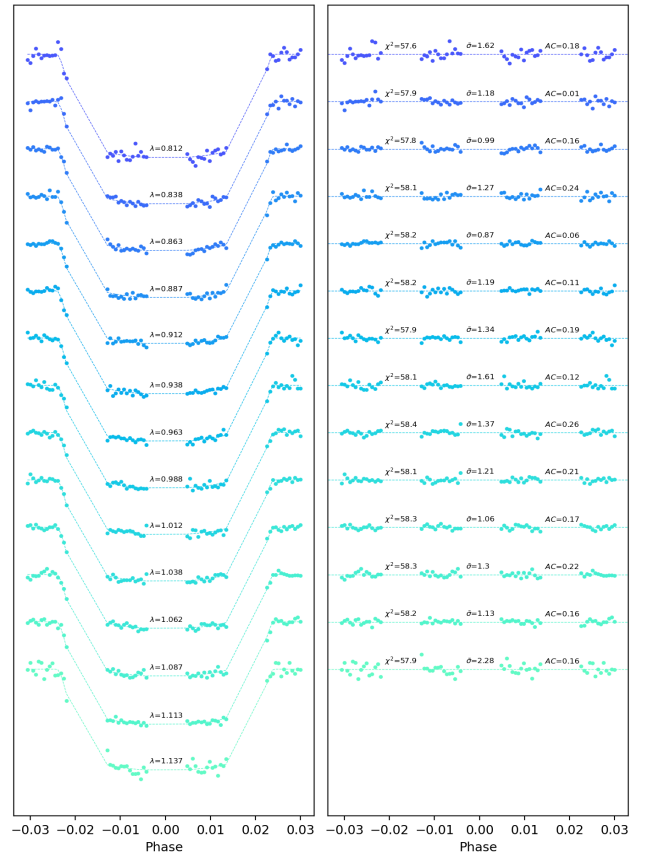
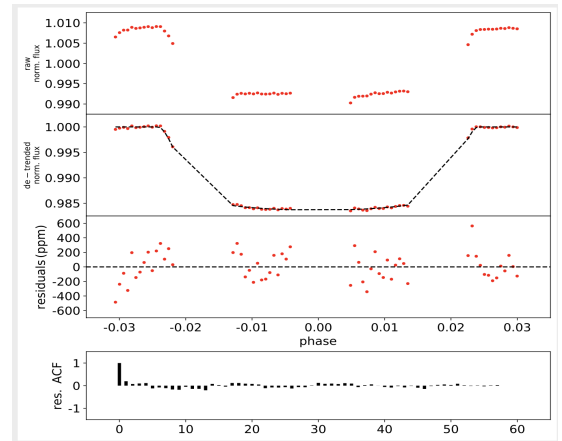


Figure 1. Top: white light curve for the HST/WFC3 G102 transmission observations of WASP-17b. First panel: raw lightcurve, after normalisation. Second panel: lightcurve, divided by the best fit model for the systematics. Third panel: residuals for best-fit model. Fourth panel: auto-correlation function of the residuals. Bottom: spectral lightcurves fitted with Iraclis for the HST/WFC3 G102 transmission spectra where, for clarity, an offset has been applied. Left panel: the detrended spectral lightcurves with the best-fit model plotted. Right panel: fitting residuals with values for the Chi-squared (χ^2), the standard deviation of the residuals with respect to the photon noise (σ) and the auto-correlation (AC) of the residuals.

² <https://github.com/ucl-exoplanets/deepARTransit>

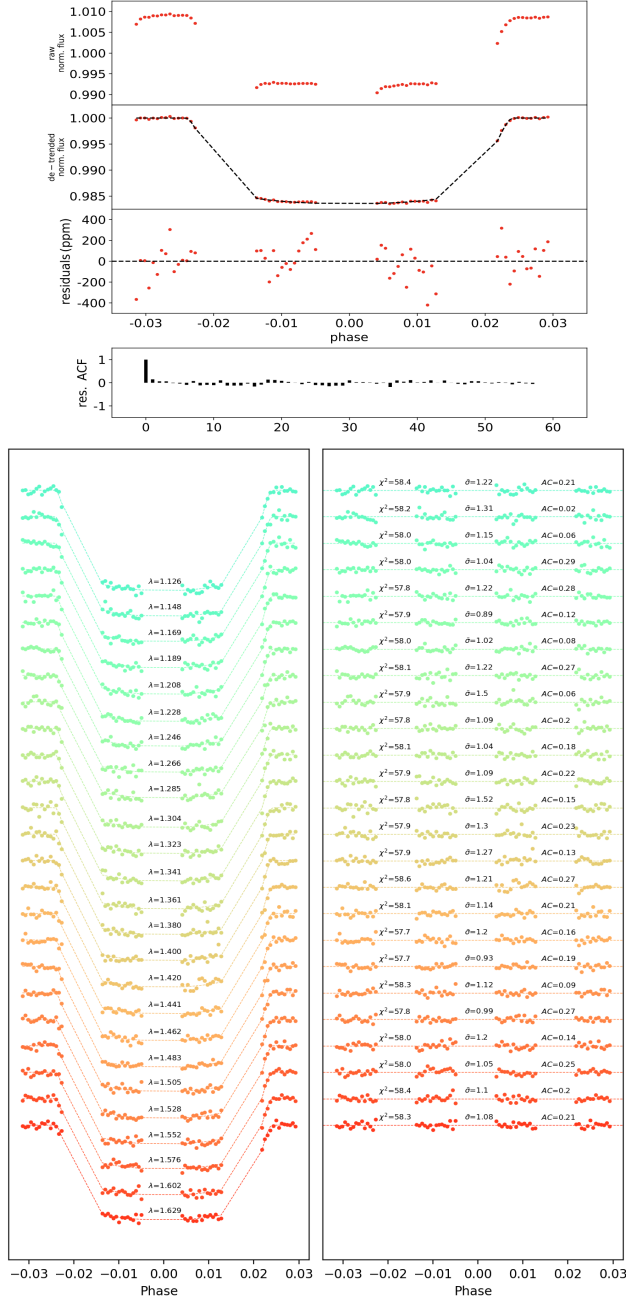


Figure 2. Top: white light curve for the HST/WFC3 G141 transmission observations of WASP-17b. First panel: raw lightcurve, after normalisation. Second panel: lightcurve, divided by the best fit model for the systematics. Third panel: residuals for best-fit model. Fourth panel: auto-correlation function of the residuals. Bottom: spectral lightcurves fitted with Iraclis for the HST/WFC3 G141 transmission spectra where, for clarity, an offset has been applied. Left panel: the detrended spectral lightcurves with the best-fit model plotted. Right panel: fitting residuals with values for the Chi-squared (χ^2), the standard deviation of the residuals with respect to the photon noise ($\bar{\sigma}$) and the auto-correlation (AC) of the residuals.

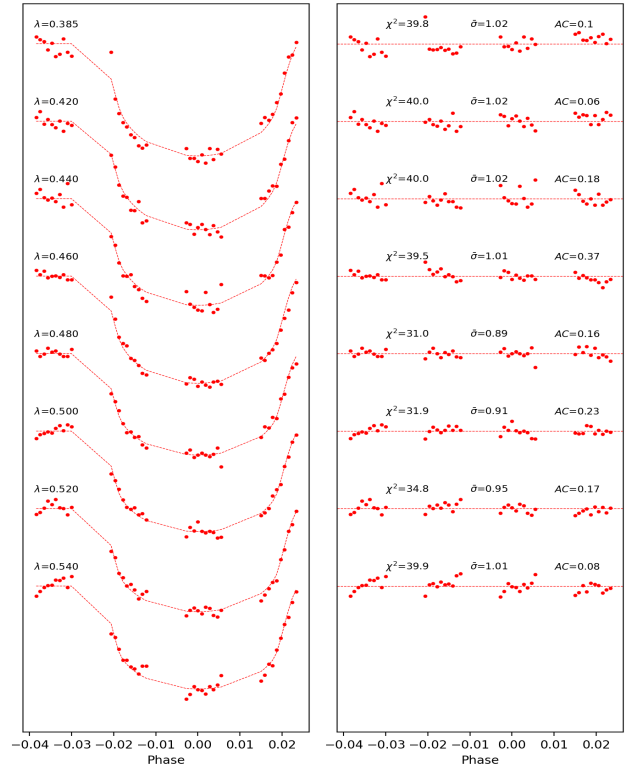
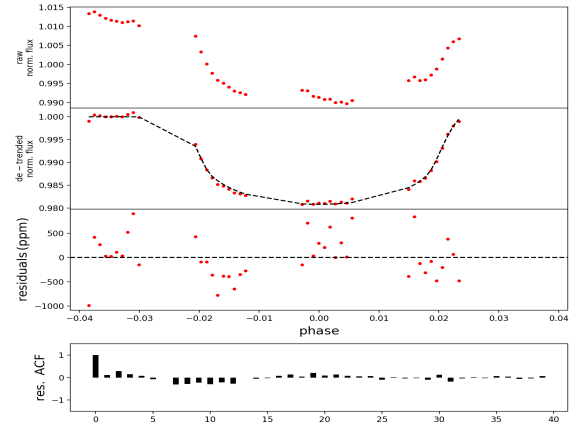


Figure 3. Top: white lightcurve for the HST/STIS G430L transmission observation taken on 2012-06-08 of WASP-17b. First panel: raw lightcurve, after normalisation. Second panel: lightcurve, divided by the best fit model for the systematics. Third panel: residuals for best-fit model. Fourth panel: auto-correlation function of the residuals. Bottom: spectral light curves fitted with Iraclis for the same observation where, for clarity, an offset has been applied. Left panel: the detrended spectral lightcurves with the best-fit model plotted. Right panel: fitting residuals with values for the Chi-squared (χ^2), the standard deviation of the residuals with respect to the photon noise ($\bar{\sigma}$) and the auto-correlation (AC) of the residuals.

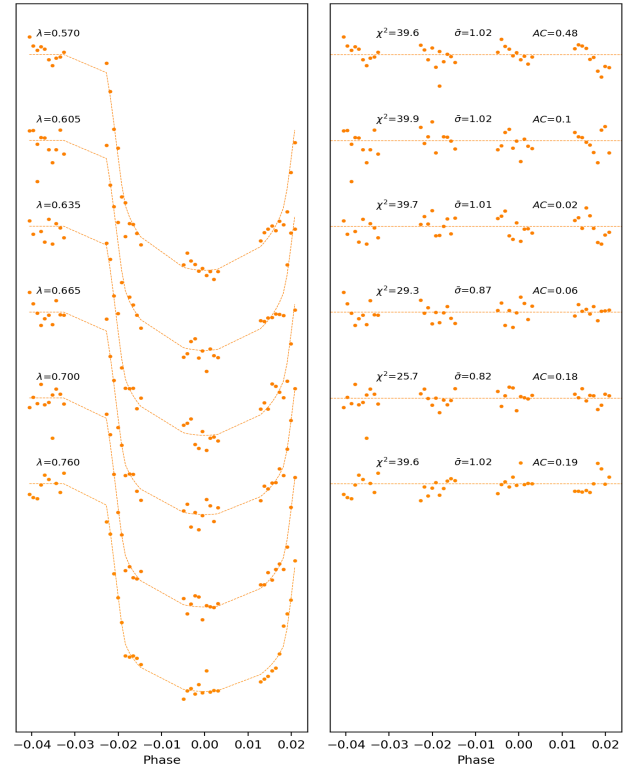
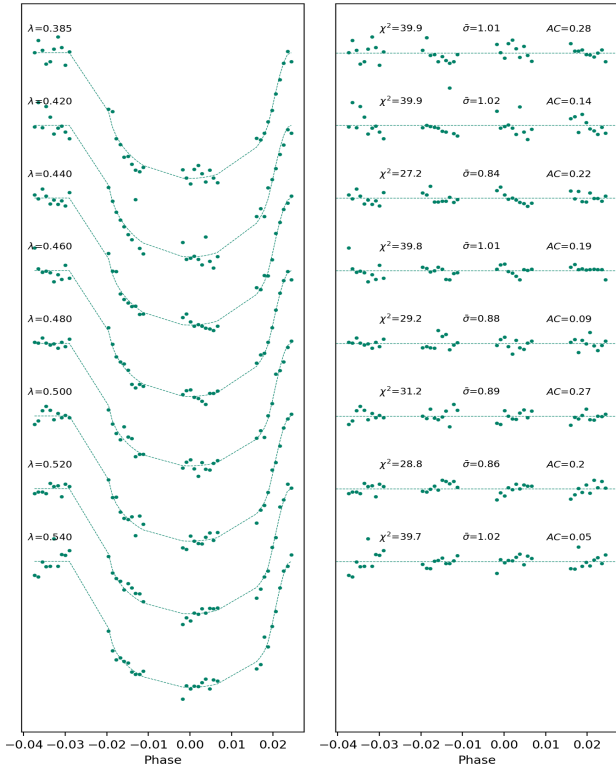
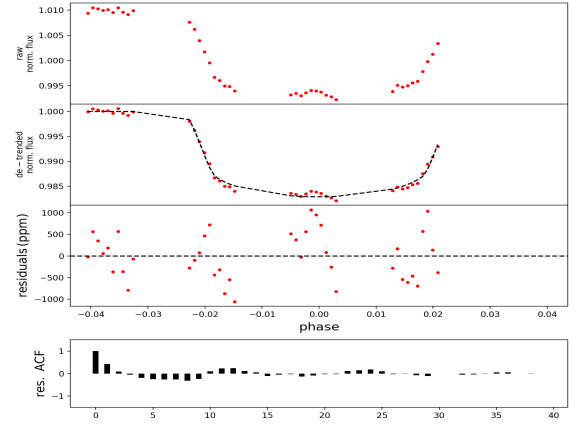
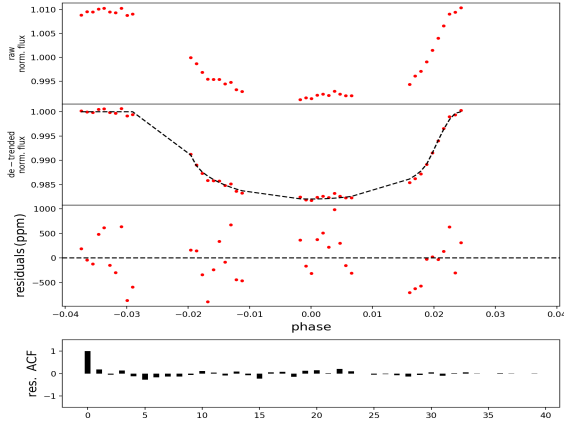


Figure 4. Top: white lightcurve for the HST/STIS G430L transmission observation taken on 2013-03-15 of WASP-17 b. First panel: raw lightcurve, after normalisation. Second panel: lightcurve, divided by the best fit model for the systematics. Third panel: residuals for best-fit model. Fourth panel: auto-correlation function of the residuals. Bottom: spectral lightcurves fitted with Iraclis for the same observation where, for clarity, an offset has been applied. Left panel: the detrended spectral lightcurves with the best-fit model plotted. Right panel: fitting residuals with values for the Chi-squared (χ^2), the standard deviation of the residuals with respect to the photon noise ($\bar{\sigma}$) and the auto-correlation (AC) of the residuals.

Figure 5. Top: white lightcurve for the HST/STIS G750L transmission observation taken on 2013-03-19 of WASP-17 b. First panel: raw lightcurve, after normalisation. Second panel: lightcurve, divided by the best fit model for the systematics. Third panel: residuals for best-fit model. Fourth panel: auto-correlation function of the residuals. Bottom: spectral lightcurves fitted with Iraclis for the same observation where, for clarity, an offset has been applied. Left panel: the detrended spectral lightcurves with the best-fit model plotted. Right panel: fitting residuals with values for the Chi-squared (χ^2), the standard deviation of the residuals with respect to the photon noise ($\bar{\sigma}$) and the auto-correlation (AC) of the residuals.

systematics is that the associated correlated noise can be inferred from the out-of-transit lightcurve and the centroid time series. First, photometric lightcurves are extracted by using a circular aperture around the center of light (with a radius of 3.25 pixels) and subtracting the background light computed at each timestep using the median flux in an annulus of inner radius equal to 15 pixels. The neural network is then trained only on the pre-ingress and post-egress parts of the lightcurves using 2-D gaussian centroid time series in order to learn only the systematics while excluding the signal. However, intermediate transit fits are performed during training on the temporary detrended lightcurve in order to keep track of the model’s progress and provide an additional stopping criterion. A first run is done with large margins around the expected ingress and egress times to ensure that the transits do not overlap with the training ranges. The margins are then refined after this first run to include 105% of the transit duration centered on the mid-transit time. In practice, the results are very stable and unaffected by the chosen margins provided these remain low (under $\approx 10\%$ of the transit duration). Several architecture and learning parameters are then tested. In both cases we find that 2 LSTM layers of 512 units and 10% dropout trained with an Adam optimiser and decay rate of $\beta = 0.95$ provide an optimal residual noise after the transit fit while avoiding overfitting. After the model was trained for 50 epochs, the best network - i.e. with the lowest residual noise - is saved along with the corresponding detrended lightcurve, obtained by dividing the raw light curve by the network’s prediction. A final transit fit is performed using a Markov Chain Monte Carlo procedure embedded in the PyLightcurve package

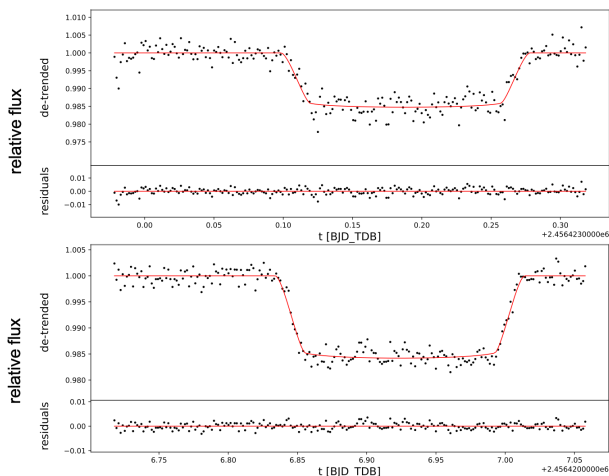


Figure 6. Detrended lightcurves and residuals for IRAC observations of WASP-17 b with channel 1 (top) and 2 (bottom).

(Tsiaras et al. 2016a). Both during and after training, the fixed planetary parameters used are those listed in Table 1 or computed using the ExoTETHyS open package (Morello et al. 2020) while the mid-transit time and R_p/R_* were let free.

2.4. Atmospheric Modelling

The spectrum resulting from our data reduction process is shown in Figure 7. Each STIS dataset is indicated with a different colour depending on the date the observation was taken on. WFC3 and Spitzer data are shown in blue and purple respectively, independently of the grism or channel employed. From the aforementioned plot we can easily notice divergent results coming from the two STIS/G430L observations, namely those taken on 2012-06-08 and 2013-03-15. For this reason we decided to model the observed spectrum in three separate cases. One scenario includes STIS visits 2012-06-08 and 2013-03-19 (from now on referred to as visit 1&3), WFC3 and Spitzer data while in the second case we aimed to model STIS visits 2013-03-15 and 2013-03-19 (visit 2&3), WFC3 and Spitzer datasets. Additionally, we investigated the spectrum constituted by the WFC3 observations only, thus discarding the inconsistencies of the STIS observations.

In each scenario, we modelled the atmosphere at the terminator of WASP-17 b using the open-source atmospheric retrieval framework TauREx3 (Al-Refaie et al. 2021). As it is customary for hot-Jupiters, we assumed this exoplanetary atmosphere to be mainly constituted by He and H in a ratio of 0.17. Given the short orbital period and an unconstrained eccentricity, we expect a tidally-locked exoplanet with an equilibrium temperature that remains constant throughout the whole orbit around the host star. Using the equation

$$T_p = T_* \sqrt{\frac{R_*}{2a}} \left(\frac{1-A}{\epsilon} \right)^{\frac{1}{4}}, \quad (1)$$

we estimated the equilibrium temperature to be $T_p = 1769$ K when assuming $A = 0.1$ and $\epsilon = 0.8$. However, since we cannot ascertain the exact albedo and emissivity of the planet, we considered some extreme cases which produce a range where we expect the planetary temperature to fall. For instance, if we assume WASP-17 b to possess an albedo of 0.5 and an emissivity of 0.7 (analogue to Jupiter), the planetary equilibrium temperature suddenly drops to $T_p = 1579$ K. If instead we consider the case of a planet that reflects a tiny amount of incoming light ($A = 0.1$) and re-emits some energy (possibly energy left over from the planet’s formation process) with $\epsilon = 0.7$, then the equilibrium temperature increases to $T_p = 1829$ K.

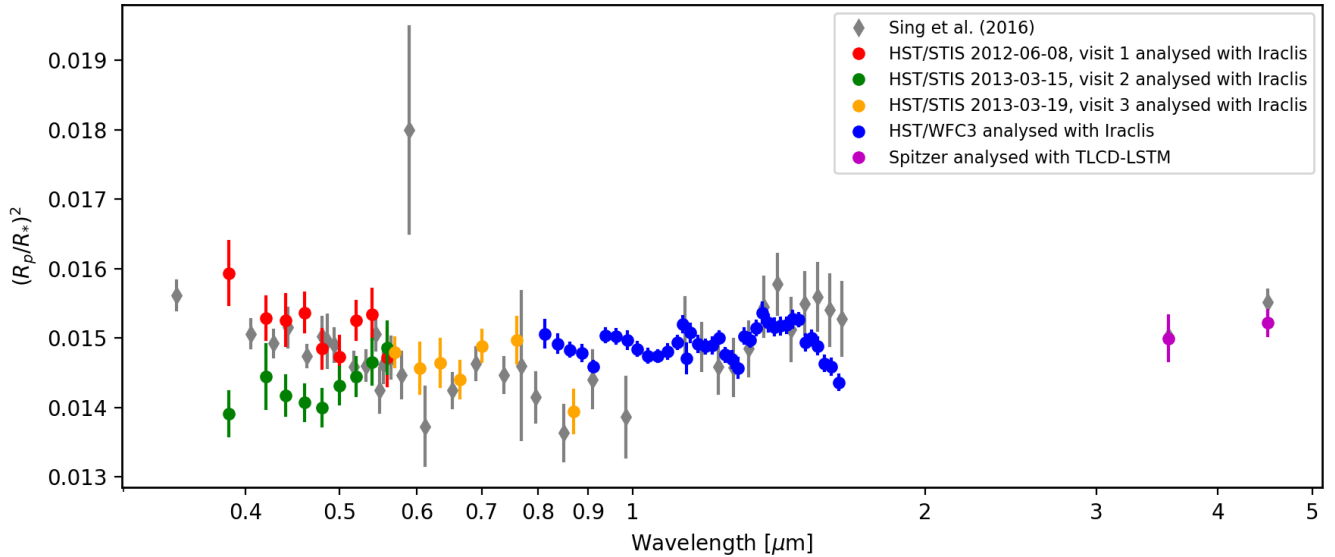


Figure 7. Transmission spectrum of WASP-17 b, constituted by HST/STIS, HST/WFC3 and Spitzer/IRAC channel 1 and 2 data analysed in this study compared to the data from Sing et al. (2016).

As a result of the broad wavelength coverage of the combined observations and the high planetary equilibrium temperature (Sharp & Burrows 2007), we explored the presence of a variety of molecular opacities, ranging from the optical (TiO (McKemmish et al. 2019), VO (McKemmish et al. 2016), FeH (Dulick et al. 2003; Wende et al. 2010), SiH (Yurchenko et al. 2018), TiH (Gharib-Nezhad et al. 2021), AlO (Patrascu et al. 2015), K (Allard et al. 2019) and Na (Allard et al. 2019)), to the near-infrared and infrared absorbers (H₂O (Polyansky et al. 2018), CH₄ (Yurchenko & Tennyson 2014), CO (Li et al. 2015), CO₂ (Rothman et al. 2010) and NH₃ (Coles et al. 2019)), by employing the linelists from the ExoMol (Tennyson et al. 2016; Chubb et al. 2021), HITEMP (Rothman et al. 2010; Rothman & Gordon 2014), HITRAN (Gordon et al. 2016; Rothman et al. 1987) and NIST (Kramida 2013) databases. Collision Induced Absorption (CIA) from H₂-H₂ (Abel et al. 2011; Fletcher et al. 2018) and H₂-He (Abel et al. 2012), Rayleigh scattering for all molecules and the presence of gray clouds and hazes modelled with the Lee et al. (2013) parameterisation were also included. In our retrievals we also modelled the contamination of the host star on the spectrum of WASP-17 b using the formalisation by Rackham et al. (2018, 2019).

We assumed a planetary atmosphere constituted by 100 layers in a plane-parallel geometry, uniformly distributed in log space between 10⁻⁵ and 10⁶ Pa. The temperature structure was modelled with an isothermal $T - p$ profile. The trace gases considered were allowed to vary freely between 10⁻¹² and 10⁻¹ in volume mix-

ing ratio, while the planetary equilibrium temperature, T_p , could vary between 500 and 3000 K. Regarding the hazes, their top pressure P_{Mie}^{top} ranged from 10⁻⁴ to 10⁶ Pa, the radius of the particles R_{Mie}^{Lee} between 10⁻³ and 1 μ m and the Mie cloud mixing ratio χ_{Mie}^{Lee} could change between -30 and -4 in log-space. Furthermore, we included a layer of gray clouds, whose top pressure could vary between 10⁻¹ and 10⁶ Pa. Lastly, the planetary radius bounds were set between 1 and 2 R_J .

We investigated the parameter space with the nested sampling algorithm MultiNest (Feroz et al. 2009b) with 750 live points and an evidence tolerance of 0.5.

2.5. Stellar Modelling

We attempted to explain the steep downward slope of STIS visit 2 observation (see Figure 7) by modelling the effect of a combination of unocculted stellar spots and faculae on the transmission spectrum of WASP-17 b. We accounted for solar size spots and faculae to be homogeneously distributed on the stellar surface. Current stellar models and observational evidence (Rackham et al. 2019, 2017; Mamajek & Hillenbrand 2008; Ciardi et al. 2011) show that the variability of F-dwarfs is $\sim 0.1\%$, with a minimum of 0.07% and a maximum of 0.36%. This is one of the lowest among all stellar spectral types, with the stellar variability being inversely proportional to the temperature of the star (McQuillan et al. 2014). Though generally FGK stars are mostly inactive and do not contaminate the transmission spectrum of the planets orbiting them, their active counter-parts do, and

great care must be taken when analysing the planetary spectra that they pollute.

According to Rackham et al. (2019), for FGK-type stars the stellar spot temperature can be calculated as:

$$T_{spot} [K] = 0.418 T_{phot} + 1620 \quad (2)$$

and the faculae temperature as:

$$T_{fac} [K] = T_{phot} + 100, \quad (3)$$

with T_{phot} being the temperature of the stellar photosphere, in our study equal to 6550 K. The spectral emission density of the heterogeneous star is modelled using the BT-Settl models (Allard et al. 2013) and the stellar spectral model grid is generated using the PHOENIX library (Husser et al. 2013). In essence, the spots and faculae are modelled as separate cooler and hotter stars respectively (Thompson et al. (in prep)). The stellar emission densities (SEDs) of the three surface components (spots, faculae and quiescent photosphere) are then combined in the ratio of their covering fractions to produce the observed disk-integrated stellar spectrum

$$S_{star,\lambda} = ((1 - F_{spot} - F_{fac}) \times S_{phot,\lambda}) + (F_{spot} \times S_{spot,\lambda}) + (F_{fac} \times S_{fac,\lambda}), \quad (4)$$

where $S_{star,\lambda}$ is the flux of the heterogeneous star at a given wavelength, $S_{phot,\lambda}$, $S_{spot,\lambda}$ and $S_{fac,\lambda}$ are the spectra of the quiet photosphere, the starspots and the faculae at the same wavelength respectively and F_{spot} and F_{fac} are the covering fractions of the spots and faculae with respect to the observed stellar disk.

Compared to the nominal transit depth, the effect of an heterogeneous star produces a wavelength-dependent offset on the transmission spectrum given by

$$\epsilon_{\lambda,s+f} = \frac{1}{1 - F_{spot} \left(1 - \frac{S_{\lambda,spot}}{S_{\lambda,phot}}\right) - F_{fac} \left(1 - \frac{S_{\lambda,fac}}{S_{\lambda,phot}}\right)}, \quad (5)$$

where F_{spot} and F_{fac} are the covering fractions of the spots and faculae and $S_{\lambda,spot}$, $S_{\lambda,fac}$ and $S_{\lambda,phot}$ are the emitted fluxes of the spots, faculae and immaculate photosphere at a given wavelength respectively. An important limitation to consider is that this simplistic method of modelling stellar active regions may be inaccurate, particularly with respect to faculae modelling as it fails to describe any centre-to-limb variations that they may exhibit or their strong dependence on magnetic field strength (Norris et al. 2017). However, given the precision of the observations in question this simplified stellar model should be sufficient to begin to investigate any potential heterogeneity displayed by WASP-17.

In our retrievals, we considered a varying spot temperature between 4000 and 5000 K, and a faculae temperature between 6600 and 7000 K. Both the spots and faculae coverage fraction bounds were set between 0.0 and 0.9 of the total stellar surface.

We tested the possibility of a variable stellar photosphere also on the spectrum comprising STIS visit 1&3, WFC3 and Spitzer observations and on the WFC3 dataset alone.

3. RESULTS

3.1. Retrievals accounting for an active star

When comparing the posteriors for each of the three cases in Figure 8, one can find common atmospheric features that are stable independently of the datasets modelled. Firstly, the planetary temperatures retrieved are within 1σ of each other and their upper bounds are inside the limits of the equilibrium temperature [1579 K; 1829 K] calculated in Section 2.5. Similarly, the planetary radii at 10 bar are compatible with one another.

All three spectra agree on a number of aspects: the presence of water in the solar/super-solar regime, which is consistent with the result from Pinhas et al. (2018), $\log_{10}(\text{H}_2\text{O}) = -4.04^{+0.91}_{-0.42}$; AIO and TiH detection in the order of 10^{-8} in volume mixing ratio; unconstrained SiH and hazes non-detection. Moreover, our results indicate a strong stellar contamination on the spectrum of WASP-17 b, in the WFC3 dataset too where we do not expect stellar activity to play a big part. In all three scenarios we retrieved a spot temperature around 4300 K, as well as spots and faculae covering fraction of the star in the order of 10-20% and 40-50% respectively. Although the faculae temperature in the transmission spectrum comprising STIS visit 1&3 is 30 K higher than what Equation 3 predicts, it is still an acceptable value compared to the large (>260 K higher than expected) and possibly nonphysical faculae temperature retrieved on the other (pink and yellow) spectra ($T_{fac} = 6912.03^{+53.69}_{-38.42}$ and $T_{fac} = 6913.46^{+55.71}_{-46.07}$).

In the pink and yellow spectrum we detect super-solar water abundances ($\log_{10}(\text{H}_2\text{O}) = -2.05^{+0.50}_{-0.81}$ and $\log_{10}(\text{H}_2\text{O}) = -2.32^{+0.53}_{-0.64}$), while the other case (blue spectrum) returns a $\log_{10}(\text{H}_2\text{O}) = -3.36^{+1.03}_{-0.53}$, being $0.72 \times$ solar and 0.87 times the result reported by Barstow et al. (2016), equal to 5×10^{-4} . Depending on the spectral scenario considered, the AIO and TiH abundances retrieved differ, yet they are compatible with each other being within their 1σ confidence band.

We retrieve conflicting results for the cloud deck. The blue and the yellow posteriors returned a cloud deck at a pressure of $\sim 10^{4.2}$ Pa corresponding to ~ 0.16 bar. In the case comprising STIS visit 2&3, the clouds top

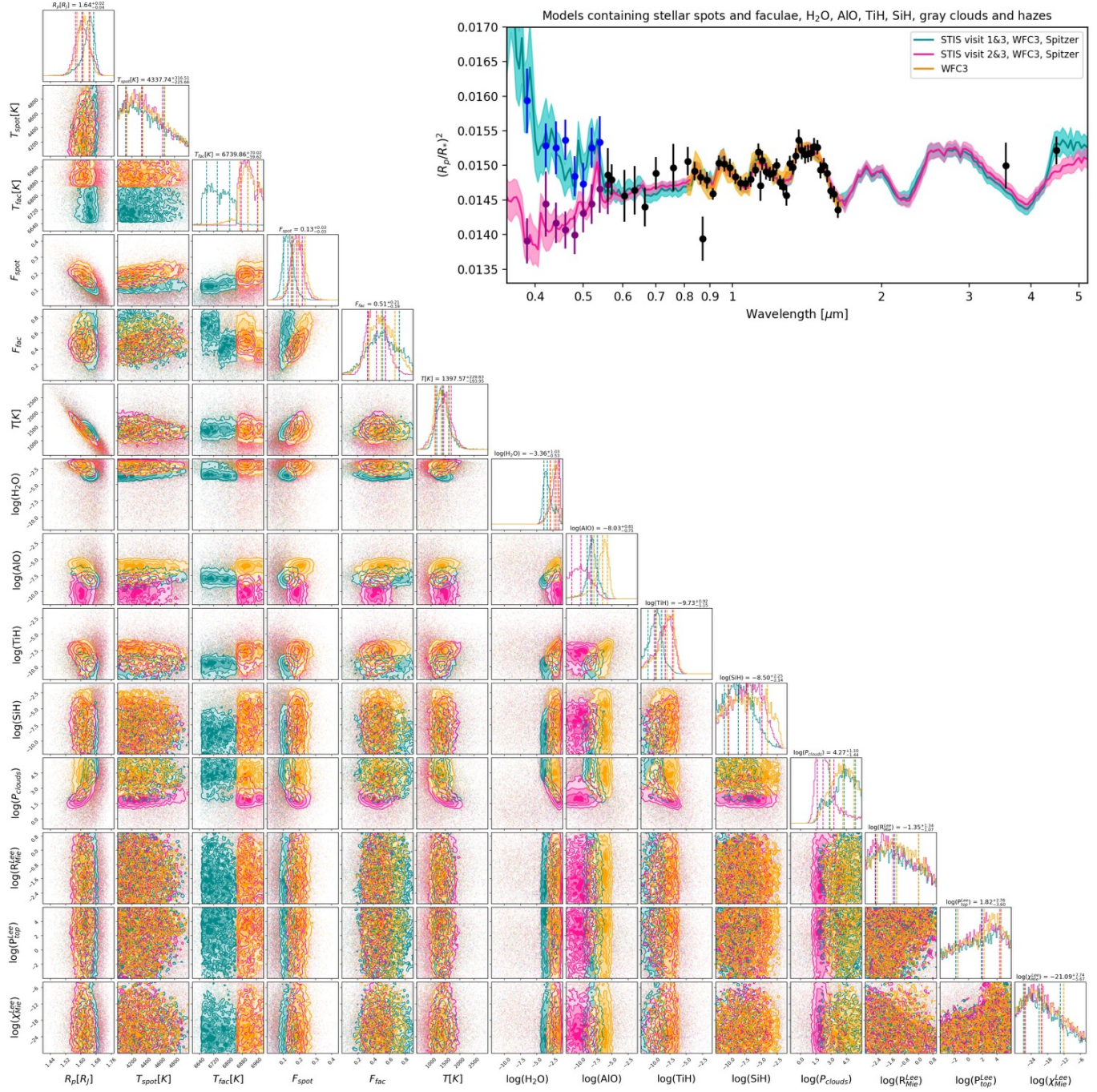


Figure 8. Posterior distributions for the transmission spectrum of WASP-17b accounting for an active star retrieved with different datasets. The reported values are those obtained with the spectrum constituted by STIS visit 1&3, WFC3, Spitzer. Inset: transmission spectra with best-fit models and their 1σ uncertainties.

pressure is higher in the atmosphere, at a pressure of 1.6 mbar. The cloud coverage found at higher altitudes could be caused by the retrieval framework trying to fit the downward slope created by the STIS visit 2 data in the optical range, which cannot be explained by any molecular absorber. The clouds cut off any molecular signature in the optical, leaving just the tip of two par-

ticular TiH and SiH signatures visible at 0.54 and 0.42 μm in the pink spectrum.

The priors used in the forward models and their retrieved values are reported in Table 2 (upper part).

3.2. Retrievals accounting for a homogeneous star

We modelled the three spectral scenarios previously identified by accounting for the same molecular and at-

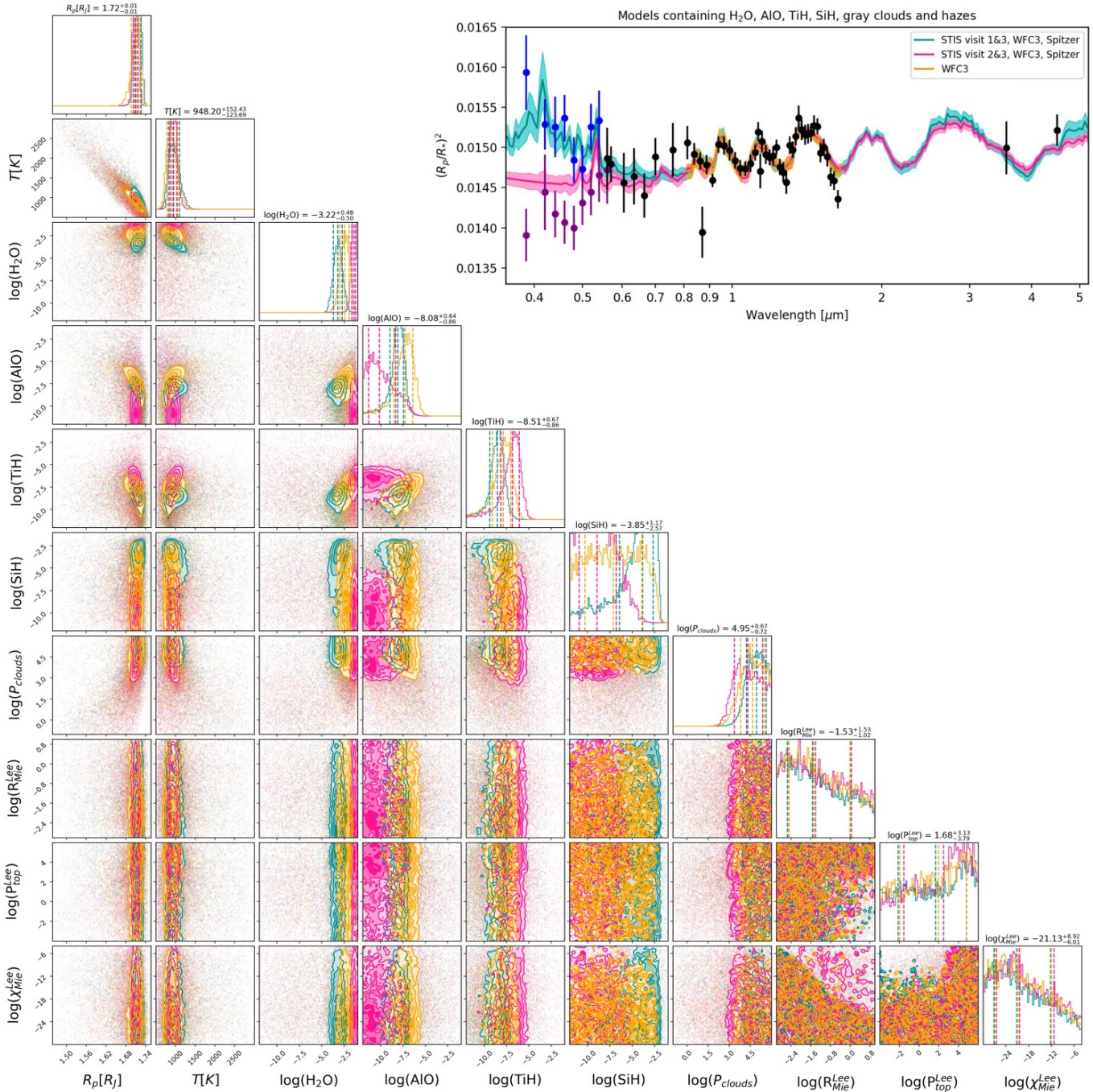


Figure 9. Posterior distributions for the transmission spectrum of WASP-17 b accounting for a homogeneous star retrieved with different datasets. The reported values are those obtained with the spectrum constituted by STIS visit 1&3, WFC3, Spitzer. Inset: transmission spectra with best-fit models and their 1σ uncertainties.

mospheric parameters. However, in this instance we modelled the star as a homogeneous body. We find that the absence of stellar activity does not impact the molecular detections, but it does affect a few of the retrieved abundances.

As in the previous case, our data suggests the presence of water, aluminium oxide and titanium hydride. Our retrievals return solar $\log(\text{H}_2\text{O}) = -3.22^{+0.48}_{-0.50}$, super solar

$\log(\text{H}_2\text{O}) = -2.45^{+0.48}_{-0.54}$ and highly super-solar $\log(\text{H}_2\text{O}) = -1.40^{+0.19}_{-0.25}$ water concentrations when modelling the blue, yellow and pink spectrum respectively. The latter two results indicate an abundance much higher than what current theories predict for hot-Jupiters (Venot et al. 2012; Venot & Agúndez 2015).

The AIO and TiH abundances retrieved from the spectrum containing only WFC3 data appear to be more

Table 2. List of the parameters, their prior bounds, the scale used and the retrieved values for the spectra including STIS visit 1&3, WFC3, Spitzer or STIS visit 2&3, WFC3, Spitzer or WFC3 only assuming an isothermal atmospheric profile.

Retrieval accounting for an active star					
Retrieved parameters	Prior bounds	Scale	STIS 1&3, WFC3, IRAC	STIS 2&3, WFC3, IRAC	WFC3
R_p [R_J]	1 ; 2	linear	$1.64^{+0.02}_{-0.04}$	$1.61^{+0.04}_{-0.03}$	1.61 ± 0.03
T_{spot} [K]	4000 ; 5000	linear	$4337.74^{+316.51}_{-225.66}$	$4344.08^{+288.40}_{-218.02}$	$4355.37^{+308.00}_{-226.38}$
T_{fac} [K]	6600 ; 7000	linear	$6739.86^{+70.02}_{-59.62}$	$6912.03^{+53.69}_{-38.42}$	$6913.46^{+55.71}_{-46.07}$
F_{spot}	0.0 ; 0.9	linear	0.13 ± 0.03	0.18 ± 0.03	0.19 ± 0.04
F_{fac}	0.0 ; 0.9	linear	$0.51^{+0.21}_{-0.19}$	0.44 ± 0.11	$0.50^{+0.17}_{-0.16}$
T [K]	500 ; 3000	linear	$1397.57^{+229.83}_{-193.95}$	$1435.55^{+266.26}_{-282.96}$	$1356.01^{+256.60}_{-220.37}$
H ₂ O	-12 ; -1	log ₁₀	$-3.36^{+1.03}_{-0.53}$	$-2.05^{+0.50}_{-0.81}$	$-2.32^{+0.53}_{-0.64}$
AIO	-12 ; -1	log ₁₀	$-8.03^{+0.81}_{-0.75}$	$-9.77^{+1.50}_{-1.38}$	$-6.43^{+0.77}_{-1.30}$
TiH	-12 ; -1	log ₁₀	$-9.73^{+0.92}_{-1.15}$	$-8.23^{+1.13}_{-1.66}$	$-7.97^{+1.04}_{-1.59}$
SiH	-12 ; -1	log ₁₀	$-8.50^{+2.25}_{-2.14}$	$-7.22^{+2.36}_{-2.78}$	$-7.03^{+3.00}_{-3.09}$
P_{clouds} [Pa]	-1 ; 6	log ₁₀	$4.27^{+1.10}_{-1.44}$	$2.21^{+1.06}_{-0.56}$	$4.14^{+1.12}_{-1.23}$
R_{Mie}^{Lee} [μm]	-3 ; 1	log ₁₀	$-1.35^{+1.34}_{-1.07}$	$-1.42^{+1.41}_{-1.02}$	$-1.23^{+1.22}_{-1.09}$
P_{Mie}^{top} [Pa]	-4 ; 6	log ₁₀	$1.82^{+2.76}_{-3.60}$	$1.92^{+2.48}_{-3.42}$	$2.21^{+2.33}_{-3.73}$
χ_{Mie}^{Lee}	-30 ; -4	log ₁₀	$-21.09^{+7.74}_{-5.67}$	$-20.13^{+7.99}_{-6.02}$	$-20.39^{+8.25}_{-6.06}$
Retrieval accounting for a homogeneous star					
Retrieved parameters	Prior bounds	Scale	STIS 1&3, WFC3, IRAC	STIS 2&3, WFC3, IRAC	WFC3
R_p [R_J]	1 ; 2	linear	1.72 ± 0.01	1.71 ± 0.01	$1.71^{+0.01}_{-0.02}$
T [K]	500 ; 3000	linear	$948.20^{+152.43}_{-123.69}$	$940.67^{+92.45}_{-80.29}$	$901.43^{+153.14}_{-116.94}$
H ₂ O	-12 ; -1	log ₁₀	$-3.22^{+0.48}_{-0.50}$	$-1.40^{+0.19}_{-0.25}$	$-2.45^{+0.48}_{-0.54}$
AIO	-12 ; -1	log ₁₀	$-8.08^{+0.64}_{-0.86}$	$-10.13^{+1.82}_{-1.20}$	$-7.28^{+0.88}_{-1.22}$
TiH	-12 ; -1	log ₁₀	$-8.51^{+0.67}_{-0.86}$	$-6.85^{+0.78}_{-1.29}$	$-7.87^{+0.87}_{-1.21}$
SiH	-12 ; -1	log ₁₀	$-3.85^{+1.17}_{-2.57}$	$-8.93^{+2.13}_{-2.00}$	$-7.11^{+3.18}_{-3.16}$
P_{clouds} [Pa]	-1 ; 6	log ₁₀	$4.95^{+0.67}_{-0.72}$	$4.32^{+1.08}_{-0.94}$	$4.66^{+0.87}_{-0.85}$
R_{Mie}^{Lee} [μm]	-3 ; 1	log ₁₀	$-1.53^{+1.53}_{-1.02}$	$-1.41^{+1.46}_{-1.08}$	$-1.48^{+1.47}_{-1.00}$
P_{Mie}^{top} [Pa]	-4 ; 6	log ₁₀	$1.68^{+3.79}_{-3.13}$	$2.46^{+2.37}_{-4.01}$	$1.97^{+2.87}_{-3.93}$
χ_{Mie}^{Lee}	-30 ; -4	log ₁₀	$-21.13^{+8.92}_{-6.01}$	$-20.36^{+9.11}_{-6.12}$	$-20.76^{+8.79}_{-6.14}$

compatible to those retrieved from the blue spectrum. However, both the AIO and the TiH results obtained from each spectra are within their respective 1σ uncertainties. SiH is still largely undetected in the spectrum constituted by STIS visit 2&3, WFC3 and Spitzer and in the spectrum containing only WFC3 data. On the other hand, exceptionally high amounts of this trace gas are detected in the spectrum constituted by STIS visit 1&3, WFC3 and Spitzer but we recognise that such huge contribution is unlikely.

Moreover, all three spectra return a consistent mean planetary radius, temperature and cloud coverage, approximately equal to $1.71 R_J$, 930 K and $\sim 10^{4.6}$ Pa respectively.

In place of stellar faculae, a Mie scattering haze could have explained the upward slope in the blue spectrum. Unfortunately, this option is refused by the retrieval, which is not able to constrain any of the aerosol parameters: particle size R_{Mie}^{Lee} , top pressure P_{Mie}^{top} , mixing

ratio χ_{Mie}^{Lee} . Even when we test the aerosols presence in the simplest model containing only water, clouds and hazes, their posterior distributions are completely unconstrained.

The priors used in the forward models and their retrieved values are reported in Table 2 (bottom part).

4. DISCUSSION

WASP-17 b has been observed, studied and modelled intensively in the past, e.g. Mandell et al. (2013); Anderson et al. (2011); Goyal et al. (2020). Despite that, this is the first time that all currently available transmission data obtained with space-based observatories has been reduced, combined and analysed consistently, allowing us to investigate the planet's atmospheric features spanning the wavelengths from the optical to the near infrared. Previous studies on WASP-17 b (Mandell et al. 2013; Sing et al. 2016; Barstow et al. 2016; Pinhas et al. 2018) analysed observations taken with

Table 3. Bayesian log-difference between different models depending on the observations fed to the retrievals.

STIS visit 1&3, WFC3, Spitzer			
Setup	Log Evidence	Sigma (discarded by)	Retrieved Temperature [K]
(1) H ₂ O, AlO, TiH, SiH, clouds, hazes, stellar activity	395.90		1397.57 ^{+229.83} _{-193.95}
(2) H ₂ O, TiO, VO, FeH, clouds, stellar activity	393.60	15.05 w.r.t. (1)	1822.35 ^{+382.41} _{-494.94}
(3) H ₂ O, AlO, TiH, SiH, clouds, hazes	389.78	3.93 w.r.t. (1)	960.66 ^{+152.33} _{-123.68}
(4) H ₂ O, TiO, VO, FeH, K, Na, clouds, hazes	383.14	5.41 w.r.t. (1)	790.32 ^{+70.19} _{-71.17}
(5) H ₂ O, AlO, TiH, clouds, hazes	388.17	4.34 w.r.t. (1)	969.77 ^{+188.02} _{-143.35}
(6) H ₂ O, TiO, VO, FeH, clouds, hazes	383.79	5.28 w.r.t. (1)	792.52 ^{+63.83} _{-69.59}

STIS visit 2&3, WFC3, Spitzer			
Setup	Log Evidence	Sigma (discarded by)	Retrieved Temperature [K]
(1) H ₂ O, AlO, TiH, SiH, clouds, hazes, stellar activity	401.14		1435.55 ^{+266.26} _{-282.96}
(2) H ₂ O, TiO, VO, FeH, clouds, stellar activity	401.42	< 1 w.r.t. (1)	1538.13 ^{+306.19} _{-346.13}
(3) H ₂ O, clouds, stellar activity	401.68	< 1 w.r.t. (1)	1351.92 ^{+234.57} _{-263.27}
(4) H ₂ O, AlO, TiH, clouds	387.88	5.5 w.r.t. (1)	945.68 ^{+98.56} _{-84.51}
(5) H ₂ O, TiO, VO, FeH, clouds	387.72	5.53 w.r.t. (1)	957.81 ^{+90.98} _{-77.41}

WFC3			
Setup	Log Evidence	Sigma (discarded by)	Retrieved Temperature [K]
(1) H ₂ O, AlO, TiH, SiH, clouds, hazes, stellar activity			1356.01 ^{+256.60} _{-220.37}
(2) H ₂ O, AlO, TiH, SiH, clouds, hazes	279.16	3.97 w.r.t. (1)	918.11 ^{+153.15} _{-116.94}
(3) H ₂ O, TiO, VO, FeH, clouds, hazes, stellar activity	284.28	2.12 w.r.t. (1)	1499.75 ^{+331.24} _{-306.95}
(4) H ₂ O, TiO, VO, FeH, clouds, hazes	276.64	4.59 w.r.t. (1)	796.60 ^{+72.10} _{-68.60}

WFC3/G141 combined with HST/STIS and Spitzer but not with WFC3/G102 (included in this work). We note that the WFC3/G141 observation employed in the aforementioned studies was taken in staring mode and lacks the post-egress part, leading to an incomplete dataset.

The combination of several datasets has its pros and cons. By coupling observations taken at different wavelengths, we are able to achieve a broad wavelength coverage, paramount to obtain more precise measurements and unambiguous molecular detection. It is extremely challenging to absolutely calibrate data obtained from different detectors, especially if each of them targets a very specific spectral range with a limited or even absent wavelength overlap (Yip et al. 2020). Moreover, each instrument creates its own distinct systematics that need to be modelled ad hoc.

The grisms mounted on the STIS detector as well as the two grisms on WFC3 share a few small portions of the wavelength space, and such wavelength overlaps allow us to confidently state that the single instrumental calibrations agree with each other. On the other hand,

between 3 and 5 μm lie the Spitzer data points, whose transit depths cannot be compared to any additional dataset. We shifted the two Spitzer data points 100 ppm up and 100 ppm down from their original position to check if the results would be considerably impacted. In either case the retrieved mean molecular abundances and other atmospheric features such as radius and temperature, fluctuate at the order of the fifth decimal figure from the initial values, implying an accurate data reduction process and stability of the results.

An additional issue to take into account when combining datasets taken months or even years apart is atmospheric variability. We must remember that planets are dynamic bodies, varying in space and time. Hence, mechanisms like star-planet interaction and global circulation processes such as polar vortexes and zonal jets can produce very strong temperature and chemical differences (Cho et al. 2003, 2021). It might not be surprising that the same planet can display contrasting spectral features at the same wavelengths, such as the two opposite spectral trends we presented between ~ 0.4 and

$\sim 0.6 \mu\text{m}$. In light of this, we must stress that the publicly available STIS observations used in this study, lack the post-egress part of the planetary transit (Figure 3, 4, 5). Missing lightcurve data strongly impacts the transit fit model, which then could potentially affect the derived transit depth, leading to discordant spectral features amongst different observations, as highlighted in Figure 7.

It is because of the discrepancies in the data that we decided to model separately the contrasting STIS datasets, in one case considering a spectrum that includes STIS visit 1&3, WFC3, IRAC; in another case we modelled the spectrum with STIS visit 2&3, WFC3, IRAC. Additionally, we employed the WFC3 observations alone to check how the results would change when we do not include the problematic STIS datasets.

To explain the unusually strong downward slope in the optical range displayed by the pink spectrum (Figure 8, inset), an active star was included in the retrieval setup. For consistency, we applied the same stellar model to the blue and yellow spectra. Potentially, STIS visit 2&3, being taken just a few days apart, were impacted by a stellar event, causing the spectrum to be best fitted by a model containing a high spots and faculae covering fraction. STIS visit 1 could have also been affected by a similar event, given that its best model favours stellar activity in place of aerosols.

Theoretically, a faculae covering fraction between 40 and 50% is unlikely in a F6-type star like WASP-17, unless we are dealing with a rare and extreme event. Moreover, we recognise that the posterior distributions between the faculae temperature and their covering fraction is degenerate (see Figure 8). This is because the retrieval is unable to distinguish between two scenarios: 1) a smaller covering fraction of hotter faculae and 2) a larger covering fraction of cooler faculae. Both scenarios result in similar stellar disk-integrated SEDs and thus introduce similar contamination features to the transmission spectrum.

There are no previous studies on the activity of the star so we are unable to compare our results with published research. However, Khalafinejad et al. (2018) mention that their attempt to identify a sodium feature in the spectrum of WASP-17 b could have been impacted by an in-transit activity of the host star, which decreased the planetary Na signal. Hence, stellar contamination cannot be excluded as an additional cause for a decreasing transit depth in the optical regime. Continuous photometric monitoring of WASP-17 is necessary to determine accurately the activity levels of the star.

When the star is treated as an homogeneous body, our retrievals of the spectrum comprising STIS visit 1&3,

WFC3 and Spitzer data results in a extremely high SiH volume mixing ratio $\log_{10}(\text{SiH}) = -3.85^{+1.17}_{-2.57}$. This result is highly unlikely and even the posteriors show that there exist quite a few solutions for which the SiH volume mixing ratio could be as low as $10^{-6.42}$. Perhaps, such high SiH abundance is due to a missing molecule which is not accounted for. Either this missing gas absorbs at the same wavelengths of SiH or it has similar absorption features. Even if we wanted to investigate this further, we do not possess all the possible molecular cross-sections and it is not feasible to test all the known molecules that absorb in the optical region. However, by inspecting the SiH results retrieved from the pink and yellow spectra, we confirm that SiH is largely unconstrained and remains undetected.

Overall, we notice that when we consider an inactive star, the retrievals struggle to fit the data points at the end of the WFC3 wavelength coverage at $\sim 1.6 - 1.8 \mu\text{m}$ and those at $0.4 - 0.55 \mu\text{m}$, especially visit 2 (see Figure 9, inset). However, independently of the datasets modelled, we detect the same trace gases (H_2O , AlO , TiH) as when accounting for a heterogeneous star. The abundances retrieved can vary, hence it is possible that the true parameter values lie somewhere in between the results retrieved from each scenario. At this stage we do not possess enough evidence to discard a particular STIS dataset in favour of another one, but the information content derived by WFC3 data alone is enough to confirm the presence of those species.

No previous study has detected any metal hydrates or oxides in the atmosphere of this particular hot-Jupiter, albeit Bento et al. (2014) searching for TiO signatures in the upper atmosphere of WASP-17 b. Theoretical studies by Fortney et al. (2008) assert the presence of TiO and VO in the atmosphere of planets with large day-night temperature contrasts. We do not exclude the presence of these trace gases but our analyses favour a model containing AlO , TiH and SiH rather than TiO , VO and FeH by a 15.05σ evidence, when applied to the spectrum comprising STIS visit 1&3, WFC3, Spitzer (Table 3). As of yet, this is the first time AlO and TiH have been suggested in the atmosphere of WASP-17 b.

During our preliminary retrievals, we tested different models containing a variety of trace gases on the spectrum displaying the upward slope, but ultimately we found that including H_2O , AlO , TiH and SiH , clouds, hazes and an active star would lead to the best results. For instance, this model is preferred by 3.93σ when compared to the same model without an active star; by 5.41σ when compared to a model with H_2O , TiO , VO , FeH , K , Na , gray clouds and aerosols. On the other hand, the spectrum containing STIS visit 2 was trickier to

model. Out of the five models tested on these data, model (1), (2) and (3) in Table 3 (middle panel) were within 0.26σ of each other, and model (5) containing H_2O , TiO , VO , FeH and gray clouds was 5.53σ away from the best-fit (model (1)). Ultimately, we used the best-fit model for the blue spectral scenario also in the other set of data and on the WFC3 data alone, to make a valid comparison between the scenarios in terms of molecular abundances. The retrievals conducted exclusively on the WFC3 data too favour a model containing H_2O , AlO , TiH , SiH , clouds, hazes, stellar spots and faculae.

Our results suggest that WASP-17 b possesses mostly a clear atmosphere, free from a thick layer of clouds and aerosols. Sing et al. (2016) report the atmosphere of this hot-Jupiter to be the clearest among the 10 exoplanets in their study, presenting distinct water features. Pinhas et al. (2018) find similar results, their spectrum being fitted best by a model containing mostly a cloudless atmosphere with a cloud/haze fraction of 0.2 and a cloud top pressure of 0.1 mbar. On the other hand, Barstow et al. (2016) report the presence of scattering aerosols at relatively high altitudes, but not so strong to reduce the size of the other molecular features. Mandell et al. (2013) also claim that their data is best fitted by a model that accounts for hazes or clouds.

We were unable to identify the alkali lines (Na, K) reported by Sing et al. (2016). The data point with an extremely large error bar that they report is not statistically significant to demonstrate the presence of sodium in the atmosphere of WASP-17 b.

We notice a difference in retrieved planetary temperature depending on the star being active or inactive. Generally, transmission studies retrieve a lower temperature compared to the calculated equilibrium temperature. Figure 11 in Skaf et al. (2020) reports the relationship between the retrieved and the equilibrium temperature for their study and for the population study in Tsiaras et al. (2018), in some cases displaying differences up to 1000 K. Our results, plotted in Figure 10, show that in the case of an active star the best-fit solution identified by Skaf et al. (2020) lies well within 1σ of the correlation between the retrieved and the equilibrium temperature. This correspondence is less evident in the case of a homogeneous star, where the results are roughly 2σ away from the best-fit, except when we consider the spectrum including STIS visit 2&3. Regardless, we do not expect the temperature at the terminator to be the same as the equilibrium temperature.

Discrepancies between the retrieved and the calculated temperatures have been analysed by several authors, e.g. Caldas et al. (2019); MacDonald et al. (2020);

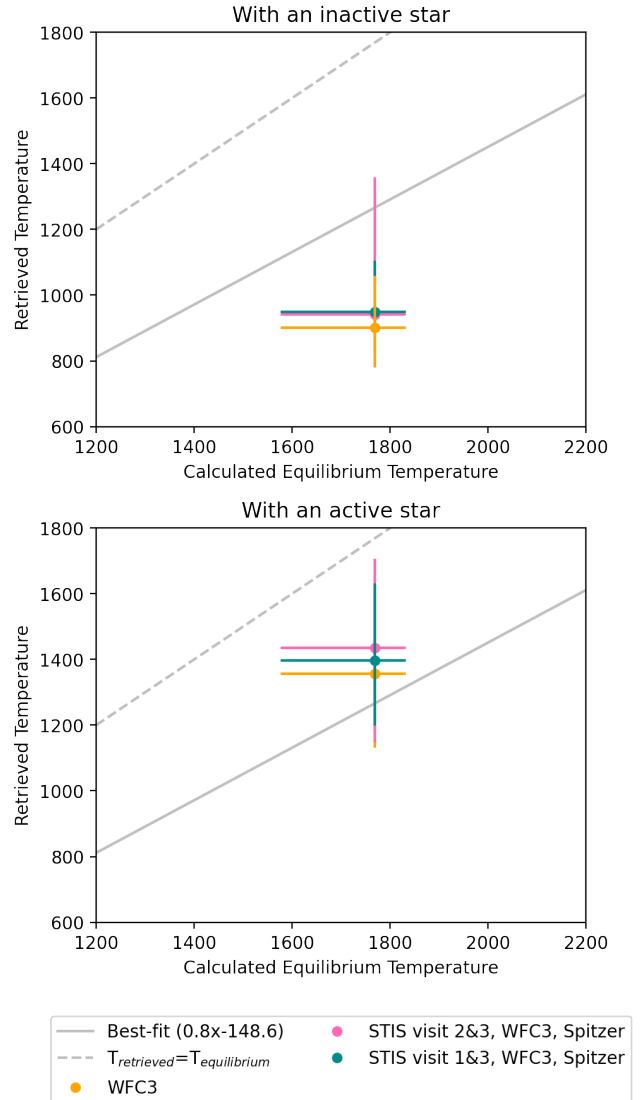


Figure 10. Retrieved temperature as a function of calculated equilibrium temperature. Top: retrievals including an inactive star. Bottom: retrievals accounting for a heterogeneous star. The correspondence between the two temperatures shown depends on the observations used during the retrieval run. Figure adapted from Skaf et al. (2020)

Pluriel et al. (2020a); Changeat et al. (2021), and found to arise from a combination of aspects: the adoption of 1D atmospheric models to describe the different molecular content of the morning and evening terminators, the use of simplified models to characterise the planets’ 3D processes and the adoption of incorrect assumptions regarding the albedo and the emissivity when calculating the planet’s equilibrium temperature. Hence, retrieving a lower temperature than calculated should not be surprising.

5. CONCLUSION

Remote-sensing studies are the only technique through which we can unveil the atmospheric characteristics of planets outside our own solar system. In recent years the *Hubble Space Telescope* has pioneered the spectroscopic investigation of exoplanets. In this study we presented the transmission spectrum of WASP-17 b observed with the Space Telescope Imaging Spectrograph and the Wide Field Camera 3 mounted on HST, and the Infrared Camera Array aboard the Spitzer Space Telescope. The Hubble raw spatially scanned spectroscopic data was reduced with Iraclis, a specialised STIS and WFC3 data reduction routine. Photometric data obtained by Spitzer was instead reduced and analysed with the TLCD-LSTM method by means of a long short-term memory network. Given the discordant results obtained for two STIS observations which cover the same wavelength range, we decided to model the spectrum of WASP-17 b in three separate cases: (a) including STIS visit 1&3, WFC3, IRAC; (b) including STIS visit 2&3, WFC3, IRAC; (c) with WFC3 only. The fully Bayesian retrieval framework TauREx3 is then employed to find the model that can best explain each spectral scenario. Retrieval results find that the best-fit model is constituted by H₂O, AlO, TiH, SiH, clouds, hazes and stellar activity in all three spectral cases. We acknowledge that the extreme stellar activity identified on the F6-type host star is unlikely, therefore we check if a model containing the same trace gases but including an homogeneous star is able to describe the three spectra. Independently of the activity of the star, our analysis indicates the presence of water in the solar/super-solar regime, AlO and TiH in the atmosphere of WASP-17 b. The atmosphere of the inflated hot-Jupiter appears to be free from both an optically thick layer of gray clouds and hazes. Given the incompleteness of the STIS lightcurves, we reckon that additional HST/STIS observations will help to improve our knowledge about the limb of this gas giant. In fact, the remarkable large scale height of WASP-17 b, makes the planet a perfect target for further atmospheric characterisation, both from the ground and by current and next generation space-based observatories such as JWST (Greene et al. 2016) and Ariel (Tinetti et al. 2018).

ACKNOWLEDGEMENTS

Data: This work is based upon observations with the NASA/ESA Hubble Space Telescope, obtained at the Space Telescope Science Institute (STScI) operated by AURA, Inc. The publicly available HST observations presented here were taken as part of proposal 12473 and 14918, led by David Sing and Hannah Wakeford respec-

tively. These were obtained from the Hubble Archive which is part of the Mikulski Archive for Space Telescopes. This work is also based in part on observations made with the Spitzer Space Telescope, which is operated by the Jet Propulsion Laboratory, California Institute of Technology, under a contract with NASA. The publicly available Spitzer data were taken as part of programme 90092 led by Jean-Michel Desert. This paper also includes data collected by the TESS mission, which are publicly available from the Mikulski Archive for Space Telescopes (MAST) and produced by the Science Processing Operations Center (SPOC) at NASA Ames Research Center (Jenkins et al. 2016). Funding for the TESS mission is provided by NASA's Science Mission directorate. We are thankful to those who operate this archive, the public nature of which increases scientific productivity and accessibility (Peek et al. 2019).

Funding: This project has received funding from the European Research Council under the European Union's Horizon 2020 research and innovation program (grant agreement No. 758892, ExoAI) and the European Union's Horizon 2020 COMPET program (grant agreement No. 776403, Exoplanets A). Furthermore, we acknowledge funding by the UK Space Agency and Science and Technology Funding Council grants ST/K502406/1, ST/P000282/1, ST/P002153/1, ST/S002634/1, ST/T001836/1, ST/V003380/1 and ST/W00254X/1.

Software: Iraclis (Tsiaras et al. 2016b), TauREx3 (Al-Refaie et al. 2021), PyLightcurve (Tsiaras et al. 2016a), Lightkurve (Cardoso et al. 2018), ExoTETHyS (Morello et al. 2020), Astropy (Price-Whelan et al. 2018), h5py (Collette 2013), emcee (Foreman-Mackey et al. 2013), Matplotlib (Hunter 2007), Multinest (Feroz et al. 2009a), Pandas (McKinney et al. 2011), Numpy (Oliphant 2006), SciPy (Virtanen et al. 2020), corner (Foreman-Mackey 2016).

REFERENCES

- Abel, M., Frommhold, L., Li, X., & Hunt, K. L. C. 2011, *The journal of physical chemistry. A*, 115, 6805–6812. <https://doi.org/10.1021/jp109441f>
- . 2012, *The Journal of chemical physics*, 136, 044319. <https://doi.org/10.1063/1.3676405>
- Al-Refaie, A. F., Changeat, Q., Waldmann, I. P., & Tinetti, G. 2021, *The Astrophysical Journal*, 917, 37. <http://dx.doi.org/10.3847/1538-4357/ac0252>
- Allard, F., Homeier, D., Freytag, B., Schaffnerberger, W., & Rajpurohit, A. 2013, arXiv preprint arXiv:1302.6559
- Allard, N., Spiegelman, F., Leininger, T., & Molliere, P. 2019, *Astronomy & Astrophysics*, 628, A120
- Anderson, D., Smith, A., Lanotte, A., et al. 2011, *Monthly Notices of the Royal Astronomical Society*, 416, 2108
- Anderson, D. R., Hellier, C., Gillon, M., et al. 2010, *ApJ*, 709, 159
- Anisman, L. O., Edwards, B., Changeat, Q., et al. 2020, *The Astronomical Journal*, 160, 233
- Arcangeli, J., Désert, J.-M., Parmentier, V., et al. 2019, *Astronomy & Astrophysics*, 625, A136
- Barstow, J. K., Aigrain, S., Irwin, P. G., & Sing, D. K. 2016, *The Astrophysical Journal*, 834, 50
- Bate, M., Lodato, G., & Pringle, J. 2010, *Monthly Notices of the Royal Astronomical Society*, 401, 1505
- Bayliss, D. D. R., Winn, J. N., Mardling, R. A., & Sackett, P. D. 2010, *ApJL*, 722, L224
- Bento, J., Wheatley, P., Copperwheat, C., et al. 2014, *Monthly Notices of the Royal Astronomical Society*, 437, 1511
- Bostroem, K., & Proffitt, C. 2011, *STIS Data Handbook*
- Bourrier, V., Lovis, C., Beust, H., et al. 2018, *Nature*, 553, 477
- Caldas, A., Leconte, J., Selsis, F., et al. 2019, *Astronomy & Astrophysics*, 623, A161
- Cardoso, J. V. d. M., Hedges, C., Gully-Santiago, M., et al. 2018, *Astrophysics Source Code Library*, ascl
- Carone, L., Mollière, P., Zhou, Y., et al. 2021, *Astronomy & Astrophysics*, 646, A168
- Changeat, Q., Al-Refaie, A. F., Edwards, B., Waldmann, I. P., & Tinetti, G. 2021, *The Astrophysical Journal*, 913, 73
- Changeat, Q., Edwards, B., Al-Refaie, A. F., et al. 2020, *The Astronomical Journal*, 160, 260
- Cho, J. Y., Menou, K., Hansen, B. M., & Seager, S. 2003, *The Astrophysical Journal Letters*, 587, L117
- Cho, J. Y., Skinner, J. W., & Thrastarson, H. T. 2021, *The Astrophysical Journal Letters*, 913, L32
- Chubb, K. L., Rocchetto, M., Yurchenko, S. N., et al. 2021, *Astronomy & Astrophysics*, 646, A21
- Ciardi, D. R., Von Braun, K., Bryden, G., et al. 2011, *The Astronomical Journal*, 141, 108
- Claret, A. 2000, *A&A*, 363, 1081
- Coles, P. A., Yurchenko, S. N., & Tennyson, J. 2019, *Monthly Notices of the Royal Astronomical Society*, 490, 4638
- Collette, A. 2013, *Python and HDF5: unlocking scientific data* ("O'Reilly Media, Inc.")
- Dulick, M., Bauschlicher Jr, C., Burrows, A., et al. 2003, *The Astrophysical Journal*, 594, 651
- Edwards, B., Changeat, Q., Baeyens, R., et al. 2020a, *The Astronomical Journal*, 160, 8
- Edwards, B., Changeat, Q., Mori, M., et al. 2020b, *The Astronomical Journal*, 161, 44
- Feng, Y. K., Line, M. R., & Fortney, J. J. 2020, *The Astronomical Journal*, 160, 137
- Feroz, F., Hobson, M., & Bridges, M. 2009a, *Monthly Notices of the Royal Astronomical Society*, 398, 1601
- Feroz, F., Hobson, M. P., & Bridges, M. 2009b, *Monthly Notices of the Royal Astronomical Society*, 398, 1601. <https://doi.org/10.1111/j.1365-2966.2009.14548.x>
- Fletcher, L. N., Gustafsson, M., & Orton, G. S. 2018, *The Astrophysical Journal Supplement Series*, 235, 24. <https://doi.org/10.3847/1538-4365/aaa07a>
- Foreman-Mackey, D. 2016, *The Journal of Open Source Software*, 1, 24
- Foreman-Mackey, D., Hogg, D. W., Lang, D., & Goodman, J. 2013, *Publications of the Astronomical Society of the Pacific*, 125, 306
- Fortney, J. J., Lodders, K., Marley, M. S., & Freedman, R. S. 2008, *The Astrophysical Journal*, 678, 1419
- Gharib-Nezhad, E., Iyer, A. R., Line, M. R., et al. 2021, *The Astrophysical Journal Supplement Series*, 254, 34
- Gordon, I., Rothman, L. S., Wilzewski, J. S., et al. 2016, in *AAS/Division for Planetary Sciences Meeting Abstracts*, Vol. 48, AAS/Division for Planetary Sciences Meeting Abstracts #48, 421.13
- Goyal, J. M., Mayne, N., Drummond, B., et al. 2020, *Monthly Notices of the Royal Astronomical Society*, 498, 4680
- Greene, T. P., Line, M. R., Montero, C., et al. 2016, *The Astrophysical Journal*, 817, 17
- Guilluy, G., Gressier, A., Wright, S., et al. 2020, *The Astronomical Journal*, 161, 19
- Guo, X., Crossfield, I. J., Dragomir, D., et al. 2020, *The Astronomical Journal*, 159, 239
- Hébrard, G., Ehrenreich, D., Bouchy, F., et al. 2011, *Astronomy & Astrophysics*, 527, L11

- Hochreiter, S., & Schmidhuber, J. 1997, *Neural computation*, 9, 1735
- Hunter, J. D. 2007, *Computing in science & engineering*, 9, 90
- Husser, T.-O., Wende-von Berg, S., Dreizler, S., et al. 2013, *Astronomy & Astrophysics*, 553, A6
- Ida, S., & Lin, D. 2004, *The Astrophysical Journal*, 616, 567
- Irwin, P. G., Parmentier, V., Taylor, J., et al. 2020, *Monthly Notices of the Royal Astronomical Society*, 493, 106
- Jenkins, J. M., Twicken, J. D., McCauliff, S., et al. 2016, in *Software and Cyberinfrastructure for Astronomy IV*, Vol. 9913, *International Society for Optics and Photonics*, 99133E
- Johnson, J. A., Winn, J. N., Albrecht, S., et al. 2009, *Publications of the Astronomical Society of the Pacific*, 121, 1104
- Khalafinejad, S., Salz, M., Cubillos, P. E., et al. 2018, *A&A*, 618, A98
- Kokori, A., Tsiaras, A., Edwards, B., et al. 2021, *Experimental Astronomy*, doi:10.1007/s10686-020-09696-3. <http://dx.doi.org/10.1007/s10686-020-09696-3>
- Kramida, A. 2013, *Fusion Science and Technology*, 63, 313
- Kreidberg, L., Line, M. R., Parmentier, V., et al. 2018, *The Astronomical Journal*, 156, 17
- Lee, J.-M., Heng, K., & Irwin, P. G. 2013, *The Astrophysical Journal*, 778, 97
- Li, G., Gordon, I. E., Rothman, L. S., et al. 2015, *The Astrophysical Journal Supplement Series*, 216, 15. <https://doi.org/10.1088/0067-0049/216/1/15>
- Lin, D. N., Bodenheimer, P., & Richardson, D. C. 1996, *Nature*, 380, 606
- MacDonald, R. J., Goyal, J. M., & Lewis, N. K. 2020, *ApJL*, 893, L43
- Mamajek, E. E., & Hillenbrand, L. A. 2008, *The Astrophysical Journal*, 687, 1264
- Mandell, A. M., Haynes, K., Sinukoff, E., et al. 2013, *The Astrophysical Journal*, 779, 128
- McKemmish, L. K., Masseron, T., Hoeijmakers, H. J., et al. 2019, *Monthly Notices of the Royal Astronomical Society*, 488, 2836
- McKemmish, L. K., Yurchenko, S. N., & Tennyson, J. 2016, *Monthly Notices of the Royal Astronomical Society*, 463, 771
- McKinney, W., et al. 2011, *Python for high performance and scientific computing*, 14, 1
- McQuillan, A., Mazeh, T., & Aigrain, S. 2014, *The Astrophysical Journal Supplement Series*, 211, 24
- Mikal-Evans, T., Sing, D. K., Goyal, J. M., et al. 2019, *Monthly Notices of the Royal Astronomical Society*, 488, 2222
- Morello, G., Claret, A., Martin-Lagarde, M., et al. 2020, *The Astronomical Journal*, 159, 75
- Morvan, M., Nikolaou, N., Tsiaras, A., & Waldmann, I. P. 2020, *The Astronomical Journal*, 159, 109
- Mugnai, L. V., Modirrousta-Galian, D., Edwards, B., et al. 2021, *The Astronomical Journal*, 161, 284
- Nagasawa, M., Ida, S., & Bessho, T. 2008, *The Astrophysical Journal*, 678, 498
- Norris, C. M., Beeck, B., Unruh, Y. C., et al. 2017, *Astronomy & Astrophysics*, 605, A45
- Oliphant, T. E. 2006, *A guide to NumPy*, Vol. 1 (Trelgol Publishing USA)
- Patrascu, A. T., Yurchenko, S. N., & Tennyson, J. 2015, *Monthly Notices of the Royal Astronomical Society*, 449, 3613
- Peek, J. E., Desai, V., White, R. L., et al. 2019, arXiv preprint arXiv:1907.06234
- Pinhas, A., Madhusudhan, N., Gandhi, S., & MacDonald, R. 2018, *Monthly Notices of the Royal Astronomical Society*, 482, 1485. <https://doi.org/10.1093/mnras/sty2544>
- Pluriel, W., Zingales, T., Leconte, J., & Parmentier, V. 2020a, arXiv preprint arXiv:2003.05943
- Pluriel, W., Whiteford, N., Edwards, B., et al. 2020b, *The Astronomical Journal*, 160, 112
- Polyansky, O. L., Kyuberis, A. A., Zobov, N. F., et al. 2018, *Monthly Notices of the Royal Astronomical Society*, 480, 2597. <https://doi.org/10.1093/mnras/sty1877>
- Price-Whelan, A. M., Sipőcz, B., Günther, H., et al. 2018, *The Astronomical Journal*, 156, 123
- Rackham, B., Espinoza, N., Apai, D., et al. 2017, *The Astrophysical Journal*, 834, 151
- Rackham, B. V., Apai, D., & Giampapa, M. S. 2018, *The Astrophysical Journal*, 853, 122
- . 2019, *The Astronomical Journal*, 157, 96
- Ricker, G. R., Winn, J. N., Vanderspek, R., et al. 2014, *Journal of Astronomical Telescopes, Instruments, and Systems*, 1, 014003
- Rothman, L. S., & Gordon, I. E. 2014, in *13th International HITRAN Conference*, 49
- Rothman, L. S., Gamache, R. R., Goldman, A., et al. 1987, *Applied optics*, 26, 4058
- Rothman, L. S., Gordon, I. E., Barber, R. J., et al. 2010, *JQSRT*, 111, 2139
- Rothman, L. S., Gordon, I., Barber, R., et al. 2010, *Journal of Quantitative Spectroscopy and Radiative Transfer*, 111, 2139

- Sedaghati, E., Boffin, H. M. J., Jeřabková, T., et al. 2016a, *A&A*, 596, A47
- Sedaghati, E., Boffin, H. M. J., Jerabková, T., et al. 2016b, *A&A*, 596, A47.
<https://doi.org/10.1051/0004-6361/201629090>
- Sharp, C. M., & Burrows, A. 2007, *The Astrophysical Journal Supplement Series*, 168, 140
- Simpson, E., Pollacco, D., Cameron, A. C., et al. 2011, *Monthly Notices of the Royal Astronomical Society*, 414, 3023
- Sing, D. K., Fortney, J. J., Nikolov, N., et al. 2016, *Nature*, 529, 59
- Skaf, N., Bieger, M. F., Edwards, B., et al. 2020, *The Astronomical Journal*, 160, 109
- Southworth, J., Hinse, T. C., Dominik, M., et al. 2012, *MNRAS*, 426, 1338
- Stassun, K. G., Collins, K. A., & Gaudi, B. S. 2017, *AJ*, 153, 136
- Stassun, K. G., Oelkers, R. J., Paegert, M., et al. 2019, *AJ*, 158, 138
- Stevenson, K. B., Line, M. R., Bean, J. L., et al. 2017, *The Astronomical Journal*, 153, 68
- Tennyson, J., Yurchenko, S. N., Al-Refaie, A. F., et al. 2016, *Journal of Molecular Spectroscopy*, 327, 73
- Tinetti, G., Drossart, P., Eccleston, P., et al. 2018, *Experimental Astronomy*, 46, 135
- TriAUD, A. H., Cameron, A. C., Queloz, D., et al. 2010, *Astronomy & Astrophysics*, 524, A25
- Tsiaras, A., Waldmann, I., Rocchetto, M., et al. 2016a, *The Astrophysical Journal*, 832, 202
- Tsiaras, A., Waldmann, I. P., Tinetti, G., Tennyson, J., & Yurchenko, S. N. 2019, *Nature Astronomy*, 3, 1086
- Tsiaras, A., Rocchetto, M., Waldmann, I., et al. 2016b, *The Astrophysical Journal*, 820, 99
- Tsiaras, A., Waldmann, I., Zingales, T., et al. 2018, *The Astronomical Journal*, 155, 156
- Venot, O., & Agúndez, M. 2015, *Experimental Astronomy*, 40, 469
- Venot, O., Hébrard, E., Agúndez, M., et al. 2012, *Astronomy & Astrophysics*, 546, A43
- Virtanen, P., Gommers, R., Oliphant, T. E., et al. 2020, *Nature methods*, 17, 261
- Wende, S., Reiners, A., Seifahrt, A., & Bernath, P. 2010, *Astronomy & Astrophysics*, 523, A58
- Winn, J. N., Johnson, J. A., Fabrycky, D., et al. 2009, *The Astrophysical Journal*, 700, 302
- Wood, P. L., Maxted, P. F. L., Smalley, B., & Iro, N. 2011, *MNRAS*, 412, 2376
- Yip, K. H., Changeat, Q., Edwards, B., et al. 2020, *The Astronomical Journal*, 161, 4
- Yurchenko, S. N., Sinden, F., Lodi, L., et al. 2018, *Monthly Notices of the Royal Astronomical Society*, 473, 5324
- Yurchenko, S. N., & Tennyson, J. 2014, *Monthly Notices of the Royal Astronomical Society*, 440, 1649–1661.
<http://dx.doi.org/10.1093/mnras/stu326>
- Zhou, G., & Bayliss, D. D. R. 2012, *MNRAS*, 426, 2483

APPENDIX

A. NETWORK PARAMETERS USED FOR DETRENDING IRAC OBSERVATIONS

Table 4. Table of parameters used for detrending IRAC observations of WASP-17 b.

	Irac Channel 1	Irac Channel 2
Program	90092	90092
Aorkey	47040000	47039488
Radius [pixels]	3.25	3.25
Centroiding method	2D Gaussian	2D Gaussian
Start of test set [BMJD TDB]	56422.595	56426.330
End of test set [BMJD TDB]	56422.783	56426.518
# layers	2	2
# units	512	512
Dropout rate	10%	10%
Adam learning rate	0.005	0.005
β decay rate	0.95	0.95

B. SPECTRAL DATA

Table 5. Reduced and fitted spectral data from the raw HST/STIS transmission data using Iraclis.

Wavelength [μm]	Transit depth [%]	Error [%]	Bandwidth [μm]	Instrument
0.385	1.593	0.045	0.050	HST STIS
0.420	1.529	0.030	0.020	HST STIS
0.440	1.525	0.037	0.020	HST STIS
0.460	1.537	0.028	0.020	HST STIS
0.480	1.484	0.027	0.020	HST STIS
0.500	1.473	0.029	0.020	HST STIS
0.520	1.525	0.027	0.020	HST STIS
0.540	1.534	0.036	0.020	HST STIS
0.560	1.472	0.041	0.020	HST STIS
0.385	1.391	0.032	0.050	HST STIS
0.420	1.444	0.046	0.020	HST STIS
0.440	1.417	0.028	0.020	HST STIS
0.460	1.407	0.026	0.020	HST STIS
0.480	1.400	0.027	0.020	HST STIS
0.500	1.431	0.026	0.020	HST STIS
0.520	1.444	0.027	0.020	HST STIS
0.540	1.466	0.033	0.020	HST STIS
0.560	1.486	0.037	0.020	HST STIS
0.570	1.479	0.021	0.040	HST STIS
0.605	1.456	0.036	0.030	HST STIS
0.635	1.464	0.034	0.030	HST STIS
0.665	1.440	0.027	0.030	HST STIS
0.700	1.488	0.022	0.040	HST STIS
0.760	1.497	0.033	0.080	HST STIS
0.870	1.394	0.031	0.140	HST STIS

Table 6. Reduced and fitted spectral data from the raw Spitzer/IRAC transmission data using TLCD-LSTM.

Wavelength [μm]	Transit depth [%]	Error [%]	Bandwidth [μm]	Instrument
3.560	1.500	0.032	0.380	Spitzer IRAC
4.500	1.521	0.018	0.560	Spitzer IRAC

Table 7. Reduced and fitted spectral data from the raw HST/WFC3 transmission data using Iraclis.

Wavelength [μm]	Transit depth [%]	Error [%]	Bandwidth [μm]	Instrument
0.813	1.506	0.019	0.025	HST WFC3
0.838	1.492	0.012	0.025	HST WFC3
0.863	1.483	0.009	0.025	HST WFC3
0.888	1.479	0.011	0.025	HST WFC3
0.913	1.459	0.007	0.025	HST WFC3
0.938	1.504	0.009	0.025	HST WFC3
0.963	1.502	0.010	0.025	HST WFC3
0.988	1.497	0.012	0.025	HST WFC3
1.013	1.484	0.009	0.025	HST WFC3
1.038	1.474	0.009	0.025	HST WFC3
1.063	1.474	0.008	0.025	HST WFC3
1.088	1.480	0.010	0.025	HST WFC3
1.113	1.493	0.009	0.025	HST WFC3
1.138	1.471	0.020	0.025	HST WFC3
1.126	1.519	0.011	0.022	HST WFC3
1.148	1.507	0.012	0.021	HST WFC3
1.169	1.491	0.011	0.021	HST WFC3
1.189	1.488	0.009	0.020	HST WFC3
1.208	1.489	0.011	0.019	HST WFC3
1.228	1.500	0.008	0.019	HST WFC3
1.246	1.476	0.009	0.019	HST WFC3
1.266	1.469	0.011	0.019	HST WFC3
1.285	1.457	0.013	0.019	HST WFC3
1.304	1.503	0.010	0.019	HST WFC3
1.323	1.497	0.009	0.019	HST WFC3
1.341	1.514	0.010	0.019	HST WFC3
1.361	1.537	0.014	0.019	HST WFC3
1.380	1.522	0.012	0.020	HST WFC3
1.400	1.516	0.011	0.020	HST WFC3
1.420	1.517	0.011	0.020	HST WFC3
1.441	1.518	0.011	0.021	HST WFC3
1.462	1.527	0.012	0.021	HST WFC3
1.483	1.526	0.009	0.022	HST WFC3
1.505	1.493	0.011	0.022	HST WFC3
1.528	1.500	0.009	0.023	HST WFC3
1.552	1.488	0.011	0.024	HST WFC3
1.576	1.463	0.010	0.025	HST WFC3
1.602	1.459	0.011	0.026	HST WFC3
1.629	1.436	0.010	0.028	HST WFC3

C. RETRIEVAL CONTRIBUTION FUNCTIONS

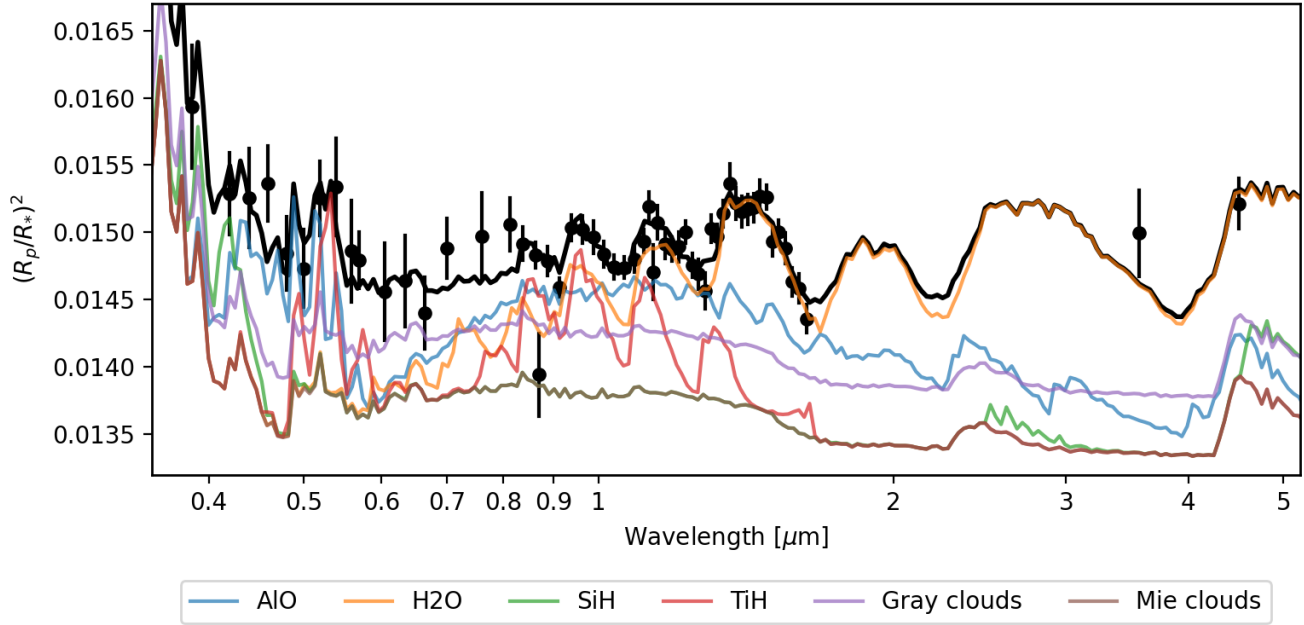


Figure 11. STIS visit 1&3, WFC3 and Spitzer data fitted by the best-fit model (black line) that includes an active star together with the contributions from the active trace gases, clouds and hazes.

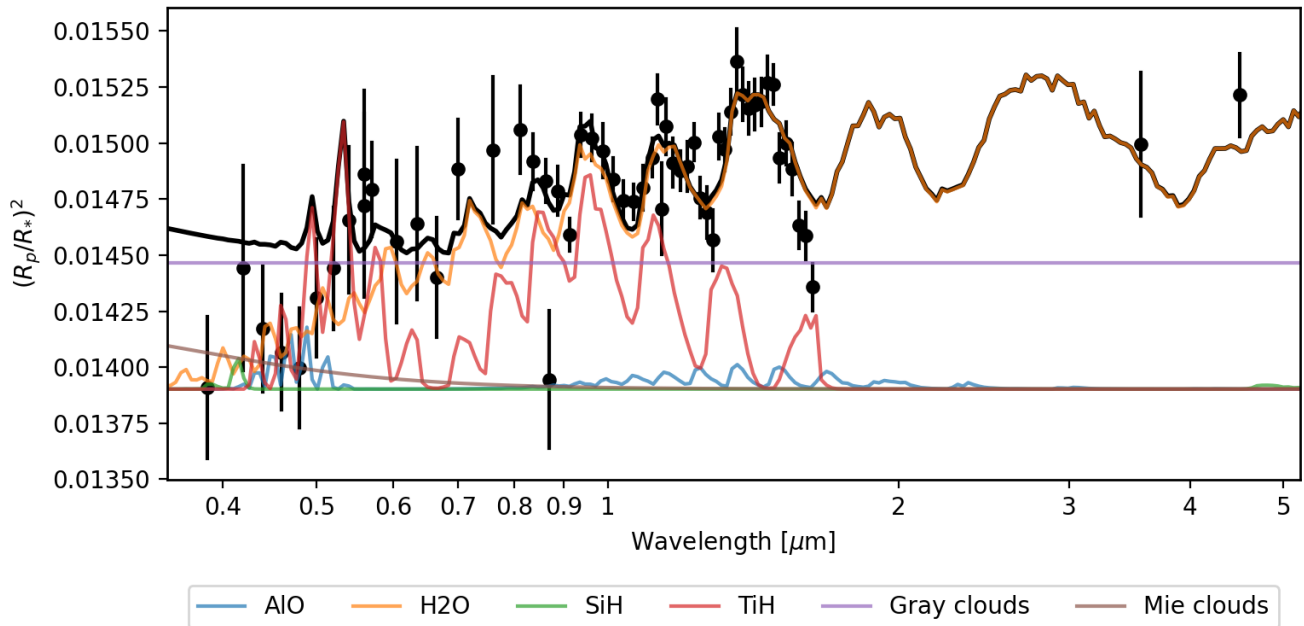


Figure 12. STIS visit 2&3, WFC3 and Spitzer data fitted by the best-fit model (black line) that includes a homogeneous star together with the contributions from the active trace gases, clouds and hazes.